Ultrasonics - Sonochemistry 62 (2020) 104847

Contents lists available at ScienceDirect

Ultrasonics - Sonochemistry

journal homepage: www.elsevier.com/locate/ultson

# A study on the spectral, microstructural, and magnetic properties of Eu–Nd double-substituted $Ba_{0.5}Sr_{0.5}Fe_{12}O_{19}$ hexaferrites synthesized by an ultrasonic-assisted approach

M.A. Almessiere[a,b], Y. Slimani[a,*], A. Demir Korkmaz[c], A. Baykal[d,*], H. Albetran[e], Tawfik A. Saleh[f], M. Sertkol[g], I. Ercan[a]

[a] Department of Biophysics, Institute for Research and Medical Consultations (IRMC), Imam Abdulrahman Bin Faisal University, P.O. Box 1982, 31441 Dammam, Saudi Arabia
[b] Department of Physics, College of Science, Imam Abdulrahman Bin Faisal University, P.O. Box 1982, 31441 Dammam, Saudi Arabia
[c] Department of Chemistry, Istanbul Medeniyet University, 34700 Istanbul, Uskudar, Turkey
[d] Department of Nanomedicine Research, Institute for Research and Medical Consultations (IRMC), Imam Abdulrahman Bin Faisal University, P.O. Box 1982, 31441 Dammam, Saudi Arabia
[e] Department of Basic Sciences, College of Education, Imam Abdulrahman Bin Faisal University, P.O. Box 1982, 31441 Dammam, Saudi Arabia
[f] Department of Chemistry, King Fahd University of Petroleum & Minerals (KFUPM), Dhahran, Saudi Arabia
[g] Deanship of Preparatory Year, Imam Abdulrahman Bin Faisal University, P.O. Box 1982, 31441 Dammam, Saudi Arabia

ARTICLE INFO

*Keywords:*
Ultrasonic sonochemistry
M-type hexaferrites
Rare earth doping
BET analysis
Magnetic belongings

ABSTRACT

In this study, an examination on the spectral, microstructural, and magnetic characteristics of Eu–Nd double-substituted $Ba_{0.5}Sr_{0.5}Fe_{12}O_{19}$ hexaferrites ($Ba_{0.5}Sr_{0.5}Nd_xEu_xFe_{12-2x}O_{19}$ (x = 0.00–0.05) HFs) fabricated by an ultrasonic-assisted approach has been presented. An UZ SONOPULS HD 2070 ultrasonic homogenizer with frequency of 20 kHz and power of 70 W was used. The chemical bonding, structure and the morphology of the products were evaluated by Fourier-Transform Infrared (FT-IR) Spectroscopy, XRD (X-ray diffraction), scanning and transmission electron microscopy and techniques. The textural properties of the prepared nanomaterials were examined by using the Brunauer-Emmett-Teller (BET) method. The magnetic properties were studied using a vibrating sample magnetometer (VSM) at room temperature (RT) and low temperature 10 K. The magnitudes of various magnetic parameters including $M_s$ (saturation magnetization), $M_r$ (remanence) and $H_c$ (coercivity) were estimated and evaluated. The M-H loops revealed the hard ferrimagnetic nature for all products at both temperatures. The $M_s$ and $M_r$ values showed a decreasing tendency with increasing degree of $Eu^{3+}$ and $Nd^{3+}$ substitutions whereas $H_c$ values displayed an increasing trend. At RT, $M_s$, $M_r$ and $H_c$ values lie in the ranges of 63.0–68.8 emu·g$^{-1}$, 24.6–39.2 emu·g$^{-1}$ and 2252.4–2782.1 Oe, respectively. At 10 K, the values of $M_s$, $M_r$ and $H_c$ lie between 87.5–97.1 emu·g$^{-1}$, 33.5–40.1 emu·g$^{-1}$ and 2060.6–2417.2 Oe, respectively. The observed magnetic properties make the prepared products promising candidates to be applied in the recording media.

## 1. Introduction

Both ferrite magnetic nanomaterials and hexaferrites (M-type) have very distinct due to that they are suitable for permanent magnet applications, high density recording media, electromagnetic wave absorption, loudspeakers, home appliances, super capacitors data storage permanent magnets, and motors etc. [1–4]. Hexaferrites have also outstanding chemical strength, remarkable uniaxial magneto crystalline anisotropy, high magnetic loss, low cost, etc. [5].

The doping of Rare Earth elements (RE) into M-type HFs results in the enhancement of the electromagnetic properties, magneto-crystalline anisotropy, coercive field and magnetization of HFs [6–8]. It is well known that RE ions enhanced the electromagnetic properties due to the presence of a 4f–3d angular momentum strong coupling. The potential field of neighboring ions in fact does not have a notable influence on the 4f shell and hence they have an enhanced coupling [9–11]. There is a boost in the number of papers containing RE doped M-type hexaferrites and they show an enhanced magnetic and microwave absorption properties [12–17].

Sonochemical synthesis approach is an efficient due to the

* Corresponding authors.
*E-mail addresses:* yaslimani@iau.edu.sa (Y. Slimani), abaykal@iau.edu.sa (A. Baykal).

https://doi.org/10.1016/j.ultsonch.2019.104847
Received 31 July 2019; Received in revised form 21 October 2019; Accepted 26 October 2019
Available online 04 November 2019
1350-4177/ 

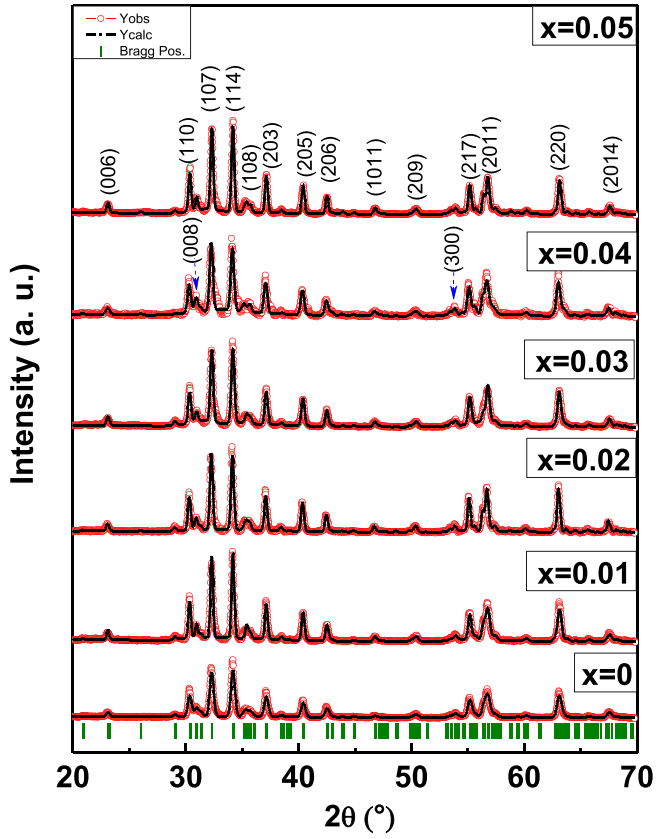


**Fig. 1.** XRD powder patterns of $Ba_{0.5}Sr_{0.5}Eu_xNd_xFe_{12-2x}O_{19}$ (x = 0.00–0.05) HFs.

homogenies dispersed phase, lessen particles size and deagglomeration of particles for improving the uniformity and stability, high-purity materials, consume-less products, saving time and improved the reaction rate [18–20].

In this paper, novel $Ba_{0.5}Sr_{0.5}Fe_{12}O_{19}$ HFs (x = 0.00–0.05) double-substituted with $Nd^{3+}$ and $Eu^{3+}$ ions have been manufactured by an ultrasonic-assisted approach.

## 2. Materials and methods

Strontium nitrate (99%), Iron Nitrate nonahydrate (98%), Barium nitrate (99%), Neodymium(III) nitrate hexahydrate (98%), Europium (III) nitrate pentahydrate (98%), and citric acid ($C_6H_8O_7$, 98%) were utilized to prepare $Ba_{0.5}Sr_{0.5}Eu_xNd_xFe_{12-2x}O_{19}$ (x = 0.00–0.05) (HFs) via an ultrasonic assisted sol–gel combustion approach. All materials, which were analytical grade purchased from Sigma Aldrich and used without further purification.

For particular synthesis of $Ba_{0.5}Sr_{0.5}Eu_xNd_xFe_{12-2x}O_{19}$ (x = 0.00–0.05) HFs, the stoichiometric amount of metal nitrate salts was suspended in deionized water (DIW) and stirred continuously at 70 °C for 2 h then its pH was attuned to 7 via $NH_3$ soln. After that, the solution was subjected to sonication 45 min using an Ultrasonic Homogenizer Q700 sonicator. To control the temperature constant (room temperature), a water bath was set-up in which the solution was kept during sonication. The powder was then washed at least 3 times with ethanol and separated from the liquid part by the use of a neodymium magnet. Finally, the powder was dried at 80 °C in air and then annealed at 1000 °C in air [20,21].

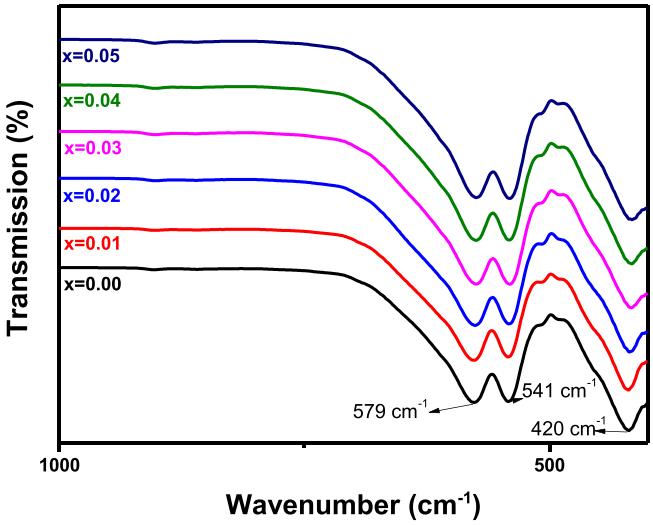


**Fig. 2.** FT-IR spectra of $Ba_{0.5}Sr_{0.5}Eu_xNd_xFe_{12-2x}O_{19}$ (x = 0.00–0.05) HFs.

An X-ray diffractometer (Rigaku, Benchtop Miniflex, with Cu-Kα irradiation) was used for the microstructural analysis. Morphological investigations were conducted by a scanning transmission electron microscope (FEI Titan 80-300 ST) equipped with EDX (energy dispersive X-ray spectroscopy) to capture the scanning electron microscopy (SEM) and transmission electron microscopy (TEM) images along with EDX analysis. A Fourier transformed infrared (FT-IR) spectrophotometer (Bruker, α-II) with an attenuated total reflectance (ATR) mode was to confirm the formation of functional groups (metal–oxygen bonds). The texture properties and porosity were determined by a Micromeritics ASAP 2020 analyzer using nitrogen adsorption–desorption at − 195 °C. Samples were heated at 160 °C for three hours for degassing and evaporation of the moisture and air gases. The specific surface area was calculated by Brunauer-Emmett-Teller (BET) method while the distribution of particle size and the pore volume determined by employing Barrett-Joyner-Halenda (BJH) procedure. To determine the magnetic traits of the products, a Physical Property Measurement System (PPMS) (Quantum Design, DynaCool-9) with a vibrating sample magnetometer (VSM) head was used.

## 3. Results and discussion

### 3.1. XRD analysis

XRD powder pattern patterns of $Ba_{0.5}Sr_{0.5}Eu_xNd_xFe_{12-2x}O_{19}$ (x = 0.00–0.05) HFs are presented in Fig. 1 which shows the hexaferrite

**Table 1**
The refined structural parameters for $Ba_{0.5}Sr_{0.5}Eu_xNd_xFe_{12-2x}O_{19}$ (x = 0.00–0.05) HFs.

| XX Content (x) | $a = b$ (Å) | $C$ (Å) | $V$ (Å)$^3$ | $c/a$ | *Crystallite Size (nm) ± 0.10* | $\chi^2$ (*chi*$^2$) | $R_{Bragg}$ |
|---|---|---|---|---|---|---|---|
| 0 | 5.887(5) | 23.109(8) | 693.70 | 3.9253 | 27.67 | 2.85 | 4.75 |
| 0.01 | 5.889(5) | 23.106(1) | 694.08 | 3.9233 | 30.66 | 2.70 | 4.79 |
| 0.02 | 5.895(6) | 23.132(6) | 696.32 | 3.9237 | 30.32 | 2.67 | 5.71 |
| 0.03 | 5.890(3) | 23.103(6) | 694.21 | 3.9223 | 27.30 | 2.30 | 4.70 |
| 0.04 | 5.895(0) | 23.125(5) | 695.97 | 3.9229 | 26.33 | 3.71 | 7.71 |
| 0.05 | 5.888(2) | 23.092(8) | 693.39 | 3.9219 | 31.49 | 2.46 | 3.91 |

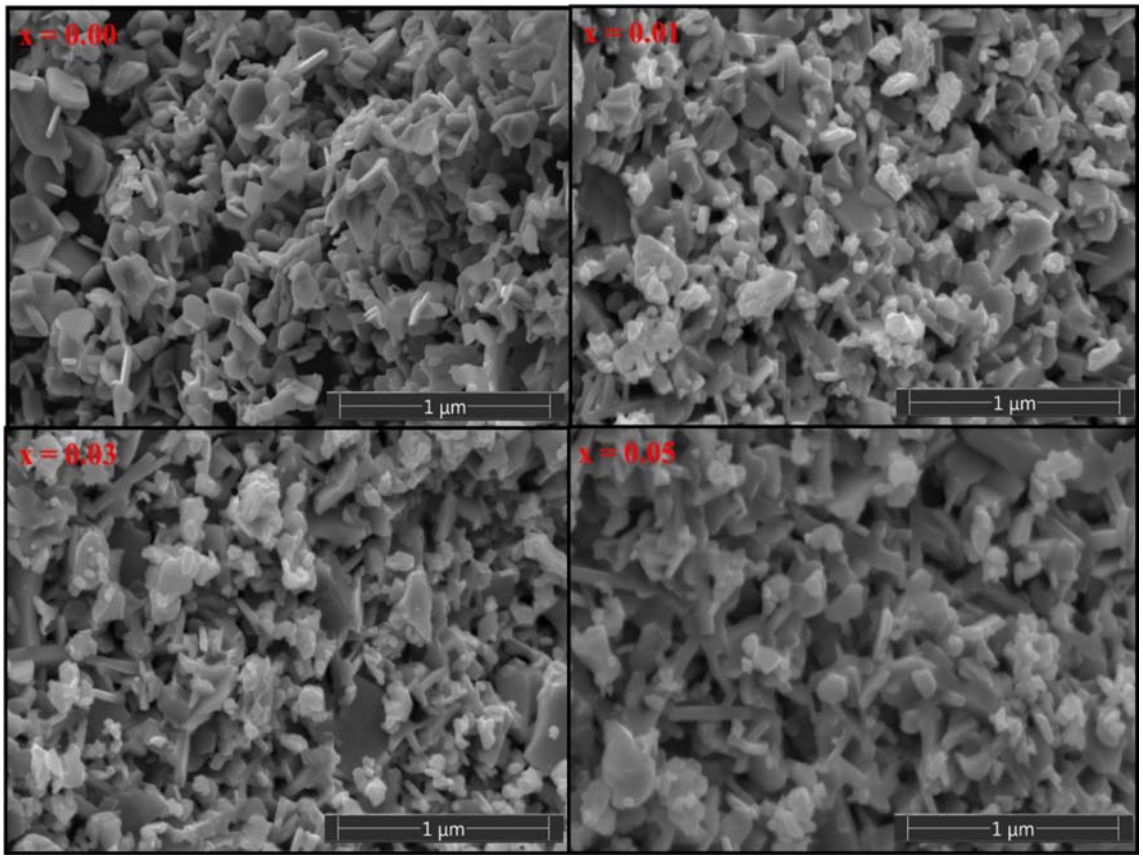


**Fig. 3.** SEM micrographs of $Ba_{0.5}Sr_{0.5}Eu_xNd_xFe_{12-2x}O_{19}$ (x = 0.00, 0.01, 0.03 and 0.05) HFs.

crystal formation for all products. The typical peaks from XRD powder patterns (having hkl values of (006), (110), (008), (107), (114), (203), (205), (206), (217), (2011) and (220)) were assigned for the M-type barium strontium hexaferrite without existence to undefined peaks (ICDD card number: 84–1531) [22–24]. The Eu-Nd ions are dissolved well in the crystal structure of Sr-Ba hexagonal ferrite.

The structural constants are calculated via Match 3! and Fullprof programs and tableted in Table 1. With increasing the Eu-Nd ratio, the lattice parameter "c" increases while "a" remains unchanged a result of the distortion inside the hexaferrite crystal by the larger ionic radii of substitution ions. The average of crystal size is evaluated by Scherrer's formula and is found to be in the range of 26–31 nm. For all compositions, the ratios of "c" to "a" are smaller than 3.98. Hence, we can say that the all of the crystal structures are M-type hexagonal ferrites.

### 3.2. FT-IR analysis

The FT-IR spectra of $Ba_{0.5}Sr_{0.5}Eu_xNd_xFe_{12-2x}O_{19}$ (x = 0.00–0.05) HFs are displayed in Fig. 2. The bands in the between 400–440 $cm^{-1}$ and 540–590 $cm^{-1}$ were assigned to the octahedral and tetrahedral sites of the metal - oxygen bonds, respectively [25]. As of the 0.645 Å ionic radius of $Fe^{3+}$ is different from those of $Nd^{3+}$ (0.983 Å) and $Eu^{3+}$ (0.947 Å), the distribution of ferric ions may change by the doping ratio within the crystal structure, which can result in a shift in the stretching bands. In addition, since the substituted ions $Eu^{3+}$ (151.96 g/mole) and $Nd^{3+}$ (144.24 g/mole) have a greater atomic mass when compared to that of $Fe^{3+}$ (55.845 g/mole) while the doping ratio were increased, the peaks positions shifted to a lower wave number [13,26].

### 3.3. SEM analysis, TEM analysis, EDX analysis and elemental mapping

SEM micrographs of $Ba_{0.5}Sr_{0.5}Eu_xNd_xFe_{12-2x}O_{19}$ (x = 0.00, 0.01, 0.03 and 0.05) HFs are depicted in Fig. 3 which confirmed the hexagonal plate structure of all products with some aggregation because of magnetic interaction among the particles. All particles are distributed homogeneously. Moreover, it is obvious that the particles size are below 40 nm, which were unchanged with while the content of the doping increases. Fig. 4 represents the EDX and elemental mapping of $Ba_{0.5}Sr_{0.5}Eu_xNd_xFe_{12-2x}O_{19}$ (x = 0.02 and 0.05) HFs. It evidently that the compositions of metal elements were near to that of the starting stoichiometric ratios of initial elements. The formation of hexagonal morphology and Sr M-type hexaferrite structure of $Ba_{0.5}Sr_{0.5}Eu_xNd_xFe_{12-2x}O_{19}$ (x = 0.01and 0.05) HFs were confirmed by TEM and high-resolution TEM (HR-TEM) analyses (Fig. 5).

### 3.4. Magnetic traits

The magnetic traits of various products were measured at 300 and 10 K through VSM at applied magnetic fields up to 9 T. The hysteresis loops of $Ba_{0.5}Sr_{0.5}Eu_xNd_xFe_{12-2x}O_{19}$ (x = 0.00–0.05) HFs are shown in Fig. 6. The magnetic parameters of the prepared samples such as $H_c$, $M_s$, and $M_r$ were deduced from the hysteresis loops (Table 2). At both RT and low temperature, it is obvious that all the prepared samples exhibit hard ferrimagnetic behavior. The $M_s$ and $M_r$ values of different products enhanced when the system was cooled to 10 K from RT (Fig. 6 and Table 2). This increase is due to the reduction of the thermal fluctuations and surface spin disorders at the surfaces of NPs [27–29]. However, $H_c$ for all prepared samples diminished with decreasing the

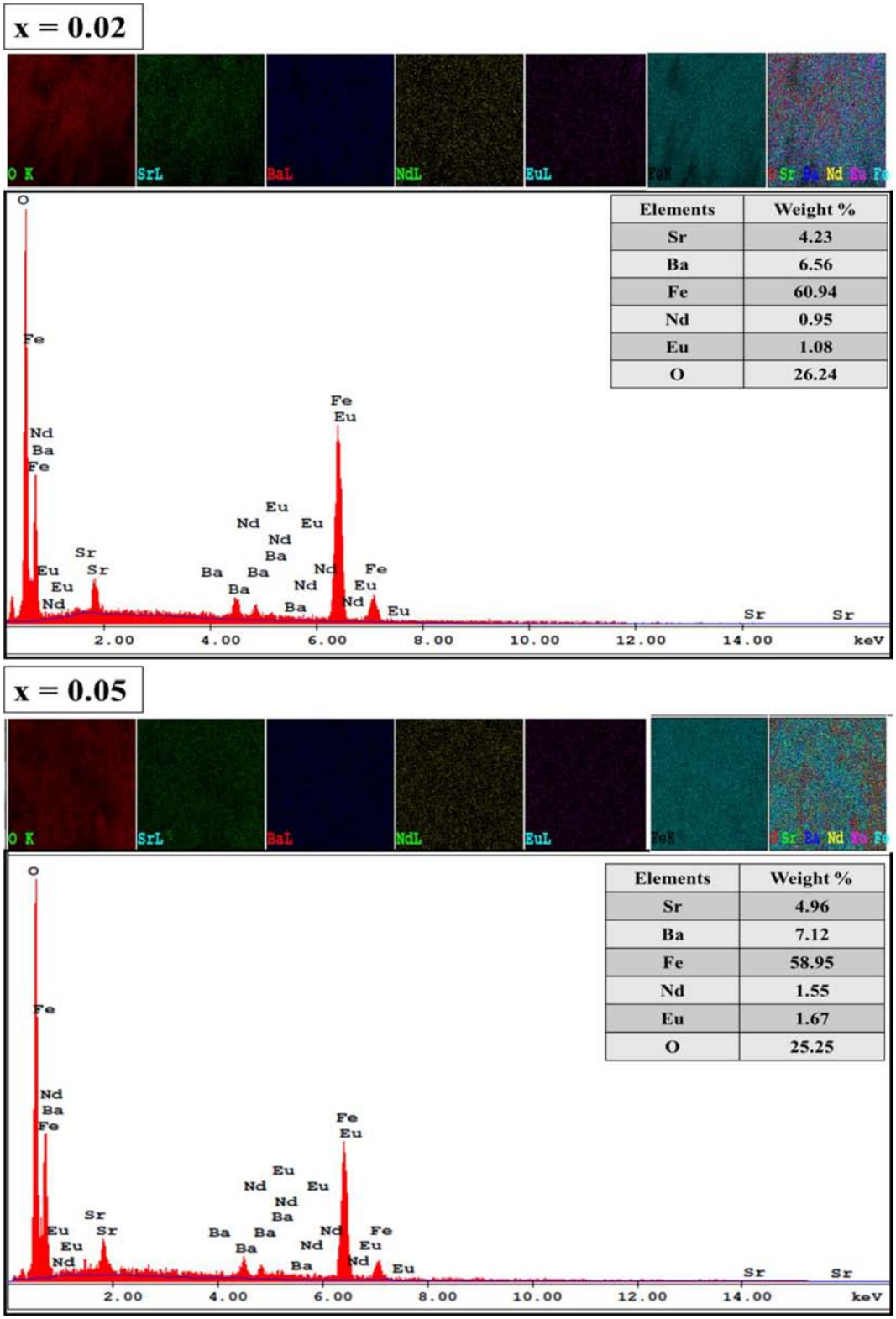


**Fig. 4.** EDX and elemental mapping of $Ba_{0.5}Sr_{0.5}Eu_xNd_xFe_{12-2x}O_{19}$ (x = 0.02 and 0.05) HFs.

temperature, which is mainly accredited to the increase in $M_s$ magnitudes and lessening in the effects of magneto-crystalline anisotropy energy with reducing the temperature [30,31].

Fig. 7 shows the influence of $Eu^{3+}$ and $Nd^{3+}$ substitutions on the $M_s$ and $M_r$ of M-type SrBa hexaferrites. At × = 0.00, when there are no substitutions of Europium and Neodymium, the values of $M_s$ are 68.8

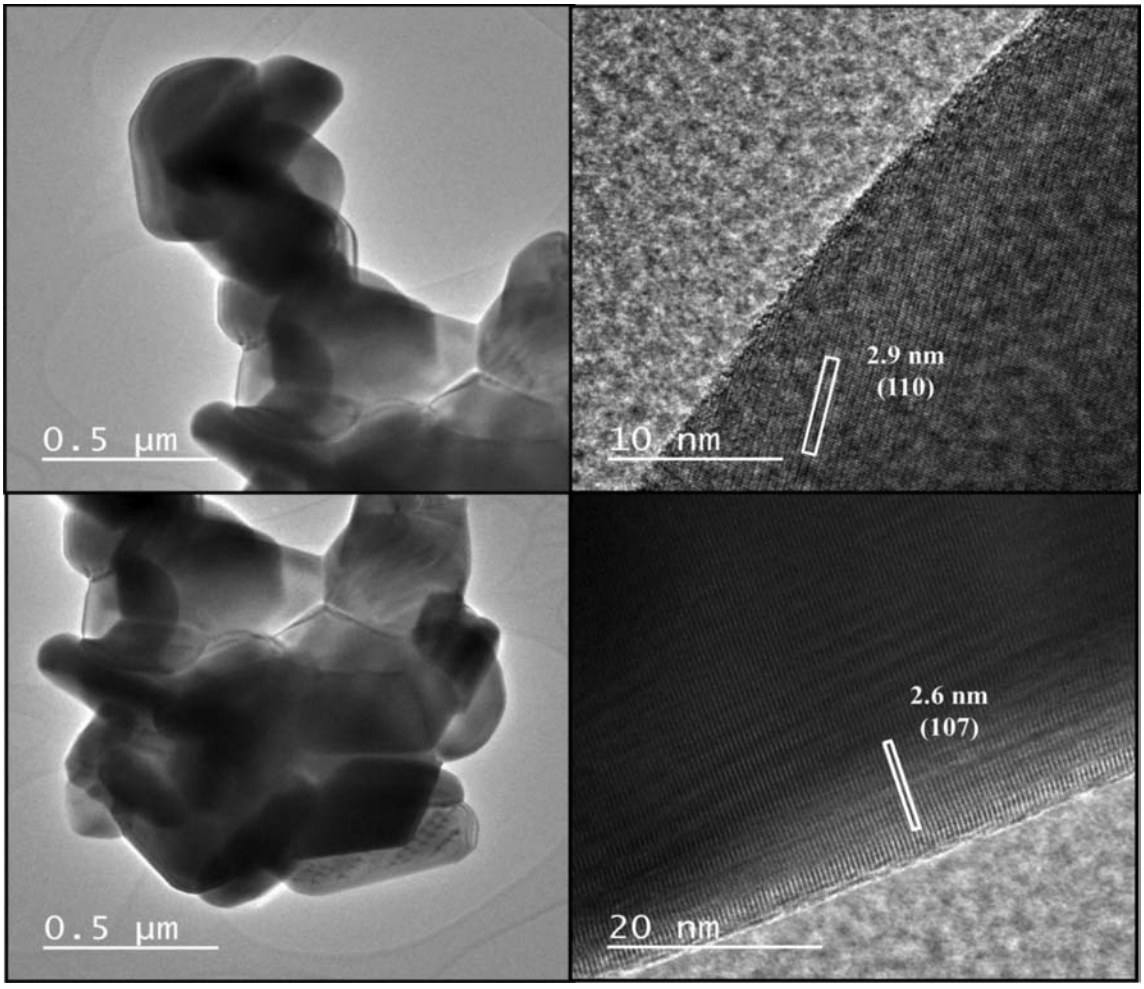


**Fig. 5.** TEM and HR-TEM of $Ba_{0.5}Sr_{0.5}Eu_xNd_xFe_{12-2x}O_{19}$ (x = 0.01 and 0.05) HFs.

and 97.1 emu·g$^{-1}$ at RT and 10 K, respectively. The undoped composition displays a retentivity $M_r$ = 39.2 and 40.1 emu·g$^{-1}$ at RT and low temperature (10 K), respectively. Recorded magnetization data are in accordance with Sr-Ba hexaferrites synthesized via chemical co-precipitation process [32,33] and greater compared to those reported in SrBa hexaferrites prepared through ceramic method [34]. A decrease of $M_s$ and $M_r$ with the substitutions of Ho and Nd has been noticed. The minimum $M_s$ and $M_r$ values at RT for × = 0.05 composition are about 63.0 and 24.6 emu·g$^{-1}$, respectively while they are about 87.5 and 33.5 emu·g$^{-1}$ at low temperature, respectively. The recorded values of magnetization for non-substituted and substituted SrBa hexaferrite samples in our study are higher when compared to those observed in $Ba_{0.5}Sr_{0.5}Co_xFe_{12-x}O_{19}$ hexaferrites [33] and in Co-W substituted SrBa hexaferrites [34]. The magnitudes of $M_s$ and $M_r$ diminished with the increase of $Eu^{3+}$ and $Nd^{3+}$ substitutions. This magnetic behavior trend of the substituted products might be influenced by the following factors. The noticed variation can be justified based on relative ionic radii of host $Fe^{3+}$ ions and the substituent $Eu^{3+}$, $Nd^{3+}$ and ions which are equal to 0.645, 0.947, and 0.983 Å, respectively. The diminishing tendency could be owing to the larger dopant $Eu^{3+}$ and $Nd^{3+}$ ions than that smaller host $Fe^{3+}$ ions. Consequently, the dissimilarity in ionic radii of $Eu^{3+}$, $Nd^{3+}$ and $Fe^{3+}$ ions generates local strains that could produce disorders and variations in the local electronic states [35,36]. Moreover, the $M_s$ and $M_r$ magnitudes are diminished because of the decrease in magnetic $Fe^{3+}$ ions with the increase of $Eu^{3+}$ and $Nd^{3+}$ substitutions. The super-exchange interaction among $Fe^{3+}$ sites lessened, which can be responsible for the decrease in the total magnetic moment because of the formation of distorted environment. Five unpaired electrons exist in the orbital 3d, where each ferric ion exhibits a 5 $\mu_B$ magnetic moment however, $Eu^{3+}$ and $Nd^{3+}$ ions have inferior magnetic moments of 3.5 $\mu_B$ and 3.6 $\mu_B$, respectively. Since the $Eu^{3+}$ and $Nd^{3+}$ ions substitute the $Fe^{3+}$ ions, there are less magnetic ions which display higher magnetic moments, and in turn this weakens $Fe^{3+}$-$O^{2-}$-$Fe^{3+}$ super-exchange interactions [37].

In a typical unit cell of hexagonal structure of M-type HFs, $Fe^{3+}$ ions possess 5 different crystal sites 2a, 2b, 12k, $4f_1$ and $4f_2$ [38,39]. In a magnetically ordered state, four $Fe^{3+}$ ions out of the twelve are in $4f_1$ and $4f_2$ sites and display ↓ spins (downward direction), whereas other eight-in 12k, 2a and 2b sites display ↑ spins (upward). The net magnetization appears from the sum of these spins. 4↑ and 4↓ spins will cancel each other and thus the remaining 4↑ $Fe^{3+}$ ions are responsible for the net magnetic moment. Some authors have concluded the net magnetization improved when $Fe^{3+}$ ions with spins-down are substituted and diminished once spins-up $Fe^{3+}$ ions are substituted [37,39]. Therefore, one could take into consideration that the $Eu^{3+}$ and $Nd^{3+}$ substitutions weakened the super-exchange interactions among Fe sites by substituting $Fe^{3+}$ ions displaying electronic spins in the upward direction. In addition, the variations in grains size with

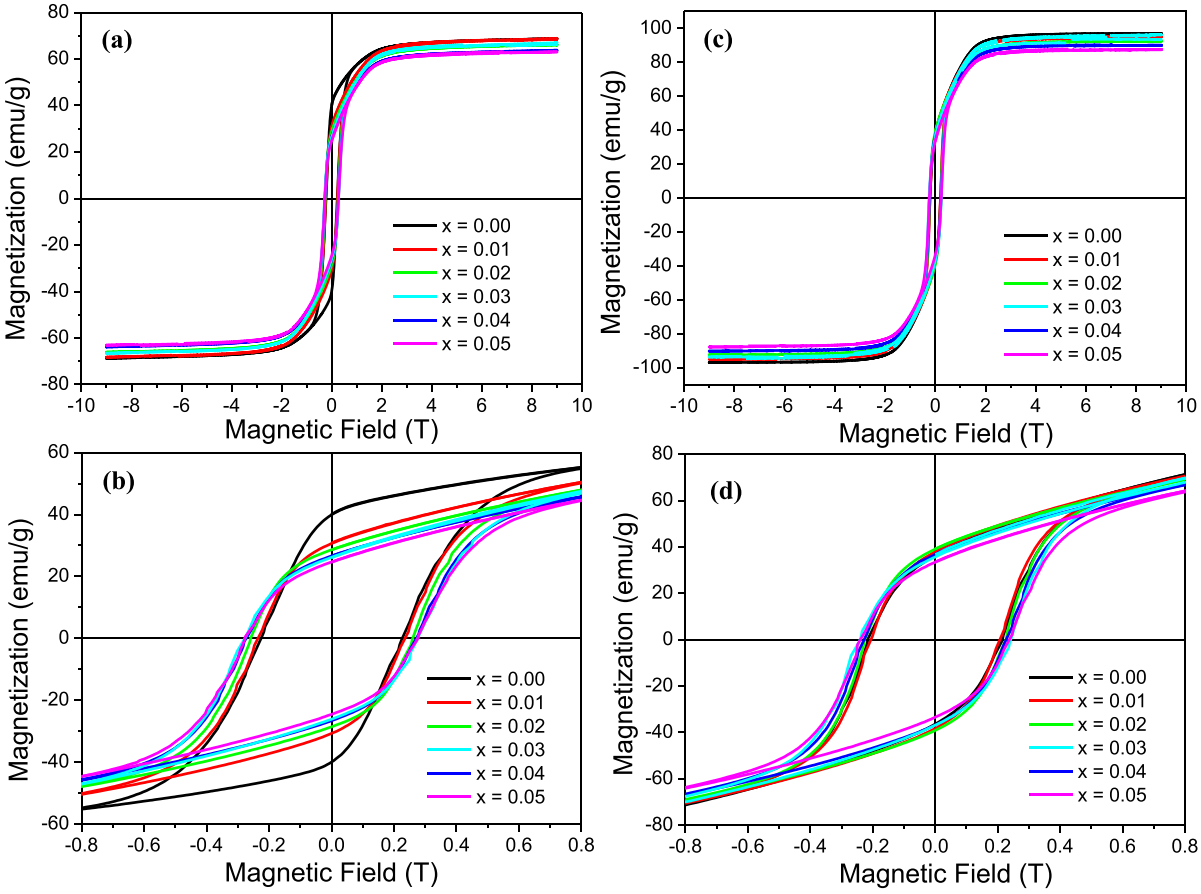


**Fig. 6.** M-H hysteresis loops of $Ba_{0.5}Sr_{0.5}Eu_xNd_xFe_{12-2x}O_{19}$ (x = 0.00–0.05) HFs performed at (a, b) T = 300 K and (c, d) 10 K.

**Table 2**
Magnetic parameters of $Ba_{0.5}Sr_{0.5}Eu_xNd_xFe_{12-2x}O_{19}$ (x = 0.00–0.05) HFs.

| x | $M_s$ (emu/g) | | $M_r$ (emu/g) | | $R = M_r/M_s$ | | $H_c$ (Oe) | | $n_B(\mu_B)$ | |
|---|---|---|---|---|---|---|---|---|---|---|
| | 300 K | 10 K | 300 K | 10 K | 300 K | 10 K | 300 K | 10 K | 300 K | 10 K |
| 0.00 | 68.8 | 97.1 | 39.2 | 40.1 | 0.483 | 0.375 | 2252.4 | 2157.4 | 13.39 | 18.89 |
| 0.01 | 68.5 | 95.0 | 30.8 | 38.1 | 0.450 | 0.413 | 2350.7 | 2060.6 | 13.35 | 18.51 |
| 0.02 | 66.7 | 93.9 | 28.6 | 36.7 | 0.429 | 0.406 | 2590.2 | 2254.2 | 13.02 | 18.33 |
| 0.03 | 66.1 | 92.5 | 26.8 | 36.4 | 0.405 | 0.397 | 2731.5 | 2278.4 | 12.93 | 18.09 |
| 0.04 | 63.7 | 90.0 | 26.4 | 35.7 | 0.414 | 0.397 | 2771.1 | 2394.6 | 12.48 | 17.63 |
| 0.05 | 63.0 | 87.5 | 24.6 | 33.5 | 0.390 | 0.383 | 2782.1 | 2417.2 | 12.36 | 17.17 |

substitution effect could explain the variation tendency in magnetization. Numerous reports showed that the magnetization diminished with reducing the grains size [40]. In our study, the crystallites size diminishes with increasing $Eu^{3+}$ and $Nd^{3+}$ substitutions, which could explain the decrease in $M_s$ and $M_r$ values.

The experimental values of the magnetic moments $n_B$ (Table 2) of all prepared samples were calculated at both at 300 and 10 K by means of the following expression [30]:

$$n_B = \frac{Molecular\ Weight \times M_s}{5585}$$

Usually, the raise in $n_B$ values is due to an intensification of super-exchange interactions between different sites [30]. A conformity in the variations of $n_B$, $M_s$ and $M_r$ was observed in the current investigation. The non-substituted SrBa hexaferrite has the highest $M_s$, $M_r$ and $n_B$ values at both 300 and 10 K. With $Eu^{3+}$ and $Nd^{3+}$ substitutions, $M_s$, $M_r$ and $n_B$ values decrease, revealing reduction in the super-exchange interactions. We also determined the *SQR* (squareness ratio) at both temperatures (Table 2). Numerous studies reported that when the *SQR* is smaller than 0.5, magnetic nanoparticles are in a single magnetic domain and when the *SQR* is equal to or greater than 0.5, they are in a multi-magnetic domain [41]. The observed values of $SQR < 0.5$ indicate all the prepared hexaferrite materials exist in a single-magnetic domain in at both temperatures.

The width of hysteresis loops reveals that the prepared products exhibit high coercive field and could be considered as hard hexagonal ferrites. The width of magnetization hysteresis loops rely on numerous reasons such as cation distribution, grain size, chemical compositions, magneto-crystalline anisotropy, porosity, etc. For non-substituted (x = 0.00) SrBa HFs, $H_c$ values are about 2252.4 and 2060.6 Oe at RT

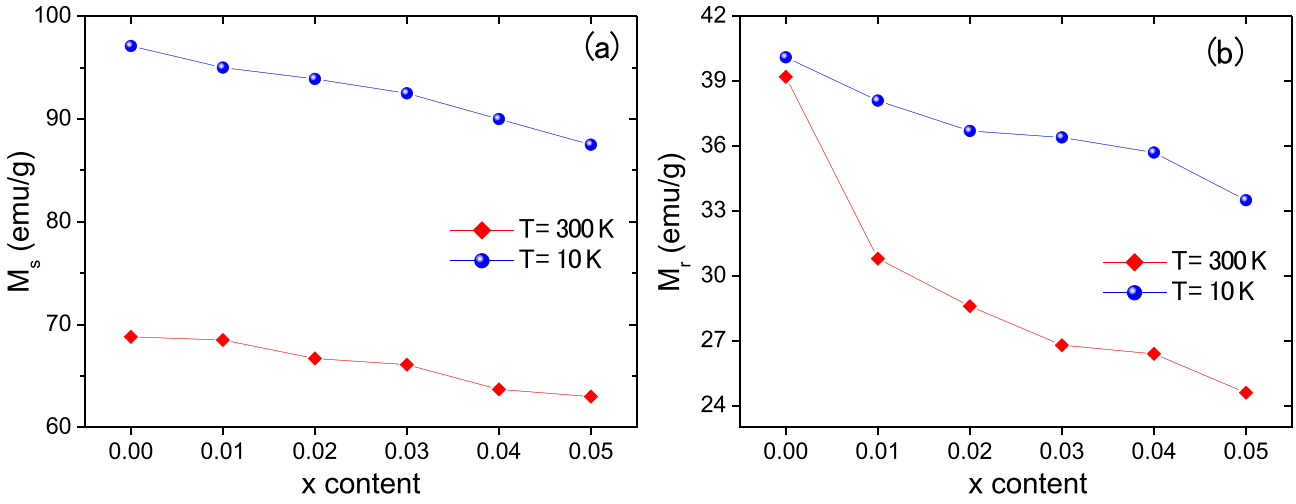


**Fig. 7.** Variations in $M_s$ and $M_r$ values with respect to $Eu^{3+}$ and $Nd^{3+}$ substitutions.

and low temperature, respectively. The non-substituted material have $H_c$ values that are high enough to be used in several applications. The $H_c$ values improved gradually with the increase of $Eu^{3+}$ and $Nd^{3+}$ substitutions (Table 2). The magnitudes of $H_c$ reached the maximum values of 2781.1 and 2417.2 Oe at x = 0.05 composition. The enhancement in coercive fields with $Eu^{3+}$ and $Nd^{3+}$ substitutions might be due to an intrinsic reason, which can be credited to a rise in the magneto-crystalline anisotropy, or extrinsic reason related to the microstructure or a contribution of both of them [37]. It should be noted that $H_c$ has a correlation with the magneto-crystalline anisotropy constant '$K$' ($H_c \propto \frac{2K}{\mu_0 M_s}$, where $\mu_0$ is the permeability of free space) [30]. Therefore, a reason of the enhancement in the coercivity might be a reason for the reinforcement in the magneto-crystalline anisotropy with $Eu^{3+}$ and $Nd^{3+}$ substitutions. Furthermore, the products containing smaller particles size have higher porosity and display higher coercivity since $H_c$ is inversely proportional to the grains size [41]. Structural and morphological investigations indicated a gradual reduction in the crystallites/grains size with $Eu^{3+}$ and $Nd^{3+}$ substitutions, which could explain the progressive enhancement in coercivity. Numerous investigations reported that a coercive field around 600 Oe is required for the longitudinal magnetic recording media [37]. Moreover, hexaferrite products could be used in the novel developing technology of perpendicular recording media when $H_c$ value is higher than 1200 Oe [37]. In the current study, all the $H_c$ values for all the prepared samples are greater than 1200 Oe, indicating that Eu and Nd doped SrBa HFs can be suitable candidates for high-density magnetic recording. Furthermore, these products could be used for absorbing materials for high frequency applications since they are hard magnets [37].

### 3.5. Textural and structural properties

Fig. 8 displays the $N_2$ physisorption isotherms collected from the textural and structural analyses and Fig. 9 shows the pore size distribution obtained from the calculations.

Based on the IUPAC classification of hysteresis loops named as H1 through H4, the loop observed in Fig. 9 is assigned to type H3 loops, attributed to mesopores (d = 2–50 nm pores, where d stands for the diameter) being present in the product [42]. In the type III isotherm in the Brunauer classification, no distinct monolayer formation is present; and the most favorable sites of the surface of macroporous or nonporous materials are surrounded by the adsorbed molecules. At high relative pressures, the absence of a limiting adsorption in the hysteresis loop is a typical characteristic of type 3 curves. When we use the desorption part of the $N_2$ isotherm and apply BJH technique, we obtain the size distribution of pores with an average pore size ranging from 9 to 17 nm along with for the nano-sized HFs. We also calculated the BET surface area of the prepared $Ba_{0.5}Sr_{0.5}Eu_xNd_xFe_{12-2x}O_{19}$ HFs. Table 3 summarizes the textural and structural parameters obtained for the prepared materials. Hierarchical factor (HiF) was estimated from the textural parameters according to the equation below as explained in the literature [43,44].

$$HiF = (V_{micro}/V_{total}) * (S_{meso}/S_{BET})$$

where $V_{micro}$ is the micropore volume, $V_{total}$ is the total pore volume, $S_{meso}$ is the mesopore surface area and $S_{BET}$ is the total surface area.

## 4. Conclusion

Eu–Nd double-substituted Ba-Sr hexaferrites were synthesized by an ultrasonic-assisted approach. The single-phase M-type hexaferrite formation for all samples were confirmed by FT-IR spectroscopy as well as XRD and scanning and transmission electron microscopy techniques. Surface properties including the textural analysis of nano hexaferrite were analyzed via Brunauer-Emmett-Teller (BET) technique. M-H loops measured at RT and 10 K showed hard ferrimagnetic character for all products. The values of $M_s$, $M_r$ and $H_c$ are between 63.0–68.8 emu/g, 24.6–39.2 emu·$g^{-1}$ and 2252.4–2782.1 Oe, respectively at RT. At 10 K, $M_s$, $M_r$ and $H_c$ values lie in the ranges of $M_s$, $M_r$ and $H_c$ lie in the ranges of 87.5–97.1 emu/g, 33.5–40.1 emu/g and 2060.6–2417.2 Oe, respectively. When the temperature decreases from RT to 10 K, $M_s$ and $M_r$ are improved, however, $H_c$ is diminished. The highest $M_s$ and $M_r$ magnitudes were observed for x = 0.00 composition. With increasing the x value, there was an increase in the total pore volume adsorbed with great uniformity of particle sizes while other textural characteristics remain similar without significant change. With increasing $Eu^{3+}$ and $Nd^{3+}$ substitution contents, $M_s$ and $M_r$ values showed a decreasing tendency. This is principally due to the different ionic radii of $Eu^{3+}$, $Nd^{3+}$ and $Fe^{3+}$ ions, generation of local strains, the super-exchange interaction weakening among $Fe^{3+}$ sites; reduction in the total magnetic moment by substituting $Fe^{3+}$ ions (5 $\mu_B$) with $Eu^{3+}$ (3.5 $\mu_B$) and $Nd^{3+}$ (3.6 $\mu_B$) ions displaying lower magnetic moments, etc. On the other hand, the coercivity is enhanced with $Eu^{3+}$ and $Nd^{3+}$

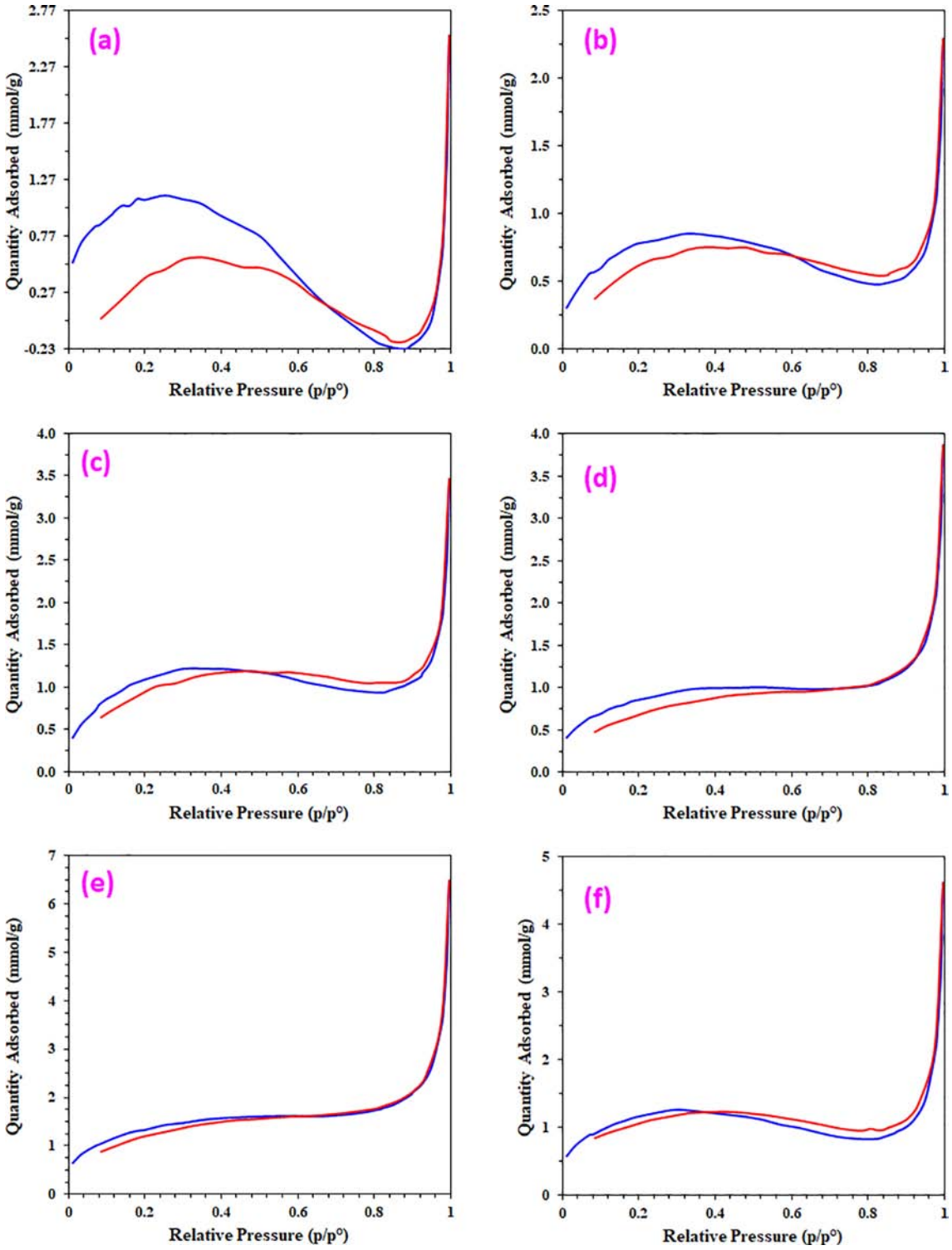


**Fig. 8.** Nitrogen physisorption isotherm plots (180 °C) of $Ba_{0.5}Sr_{0.5}Eu_xNd_xFe_{12-2x}O_{19}$ (x = 0.00–0.05) HFs (a) x = 0.00, (b) x = 0.01, (c) x = 0.02, (d) x = 0.03, (e) x = 0.04; (f) x = 0.05.

substitutions, which is associated with the increase in the magneto-crystalline anisotropy as well as a reduction in the crystallite size. Furthermore, the observed magnetic properties in this study could make the prepared products promising candidates in the high-density recording media devices along with high frequency applications.

## Declaration of Competing Interest

The authors declare that they have no known competing financial interests or personal relationships that could have appeared to influence the work reported in this paper.

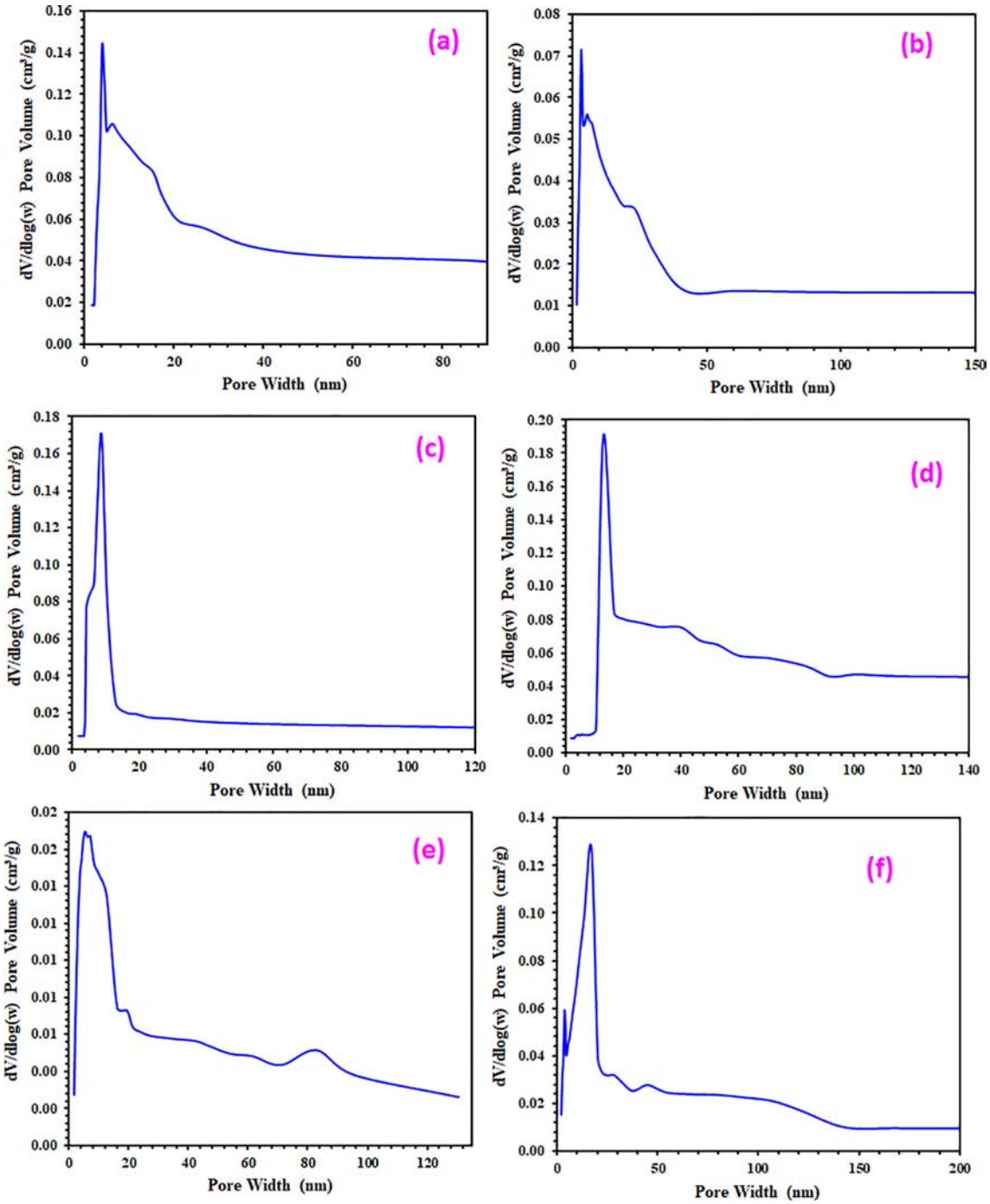


**Fig. 9.** Pore side distribution of $Ba_{0.5}Sr_{0.5}Eu_xNd_xFe_{12-2x}O_{19}$ (x = 0.00–0.05) HFs (a) x = 0.00, (b) x = 0.01, (c) x = 0.02, (d) x = 0.03, (e) x = 0.04; (f) x = 0.05.

**Table 3**
Textural and structural properties of $Ba_{0.5}Sr_{0.5}Eu_xNd_xFe_{12-2x}O_{19}$ (x = 0.00–0.05) HFs.

| X | $S_{BET}$ ($m^2$/g) | $S_{micro}$[a] ($m^2$/g) | $S_{meso}$[b] ($m^2$/g) | $V_t$[c] ($cm^3$/g) | $V_{micro}$ ($cm^3$/g[a]) | $d_p$ (nm)[d] | APS (nm)[e] | HF[f] |
|---|---|---|---|---|---|---|---|---|
| 0.00 | 3.1494 | 5.7561 | 2.3791 | 0.00258 | 0.00062 | 17.4907 | 99.7 | 0.1802 |
| 0.01 | 2.6658 | 4.4966 | 3.4018 | 0.00269 | 0.0003 | 9.8164 | 73 | 0.1421 |
| 0.02 | 3.9957 | 6.4508 | 4.9225 | 0.00416 | 0.00047 | 9.1187 | 72 | 0.1396 |
| 0.03 | 2.9076 | 4.5992 | 3.3317 | 0.00474 | 0.00014 | 12.1891 | 67 | 0.0341 |
| 0.04 | 4.524 | 7.2034 | 5.223 | 0.008 | 0.00021 | 12.8809 | 63 | 0.0296 |
| 0.05 | 4.0313 | 4.0313 | 4.3314 | 0.00543 | 0.00093 | 14.1855 | 59 | 0.1841 |

[a] Micropore area/volume calculated using the *t*-plot.
[b] External surface area calculated using the *t*-plot.
[c] Total pore volume adsorbed at $p/p^0 = 0.95$.
[d] BJH Adsorption average pore width (4 V/A).
[e] Average particle size (APS).
[f] Hierarchical factor (HF); $HF = (V_{micro}/V_{total}) * (S_{meso}/S_{BET})$.

## References


[1] D. Makovec, M. Komelj, G. Drazic, B. Belec, T. Gorsak, S. Gyergyek, D. Lisjak, Incorporation of Sc into the structure of barium-hexaferrite nanoplatelets and its extraordinary finite-size effect on the magnetic properties, Actamaterialia 172 (2019) 84–91.

[2] A. Manikandan, M. Durka, S.A. Antony, Magnetically recyclable spinel $Mn_xZn_{1-x}Fe_2O_4$ ($0.0 \le x \le 0.5$) nano-photocatalysts, Adv. Sci. Eng. Med. 7 (2015) 33–46.

[3] G. Mathubala, A. Manikandan, S.A. Antony, P. Ramar, Enhanced photocatalytic activity of spinel $Cu_xMn_{1-x}Fe_2O_4$ nanocatalysts for the degradation of methylene blue dye and opto-magnetic properties, Nanosci. Nanotechnol. Lett. 8 (2016) 375–381.

[4] M.F. Valan, A. Manikandan, S.A. Antony, A novel synthesis and characterization studies of magnetic $Co_3O_4$ nanoparticles, J. Nanosci. Nanotechnol. 15 (2015) 4580–4586.

[5] S.S. Veisi, M. Yousefi, M.M. Amini, A.R. Shakeri, M. Bagherzadeh, Magnetic and microwave absorption properties of Cu/Zr doped M-type Ba/Sr hexaferrites prepared via sol-gel auto-combustion method, J. Alloy. Compd. 773 (2019) 1187–1194.

[6] N. Yasmin, M. Mirza, S. Muhammad, M. Zahid, M. Ahmad, M.S. Awan, A. Muhammad, Influence of samarium substitution on the structural and magnetic properties of M-type hexagonal ferrites, J. Magn. Magn. Mater. 446 (2018) 276–281.

[7] K. Elayakumar, A. Dinesh, A. Manikandan, M. Palanivelu, G. Kavitha, S. Prakash, R.T. Kumar, S.K. Jaganathan, A. Baykal, Structural, morphological, enhanced magnetic properties and antibacterial bio-medical activity of rare earth element (REE)cerium ($Ce^{3+}$) doped $CoFe_2O_4$ nanoparticles, J. Magn. Magn. Mater. 476 (2019) 157–165.

[8] K. Elayakumar, A. Manikandan, A. Dinesh, K. Thanrasu, K.K. Raja, R.T. Kumar, Y. Slimani, S.K. Jaganathan, A. Baykal, Enhanced magnetic property and antibacterial biomedical activity of $Ce^{3+}$ doped $CuFe_2O_4$ spinel nanoparticles synthesized by sol-gel method, J. Magn. Magn. Mater. 478 (2019) 140–147.

[9] I. Sadiq, S. Naseem, M.N. Ashiq, M.A. Iqbal, I. Ali, M.A. Khan, Spin canting effect and microwave absorption properties of Sm-Mn substituted nanosized material, J. Magn. Magn. Mater. 395 (2015) 159–165.

[10] L. Wang, J. Zhang, Q. Zhang, N. Xu, J. Song, XAFS and XPS studies on site occupation of $Sm^{3+}$ ions in Sm doped M-type$BaFe_{12}O_{19}$, J. Magn. Magn. Mater. 377 (2015) 362–367.

[11] I.A. Auwal, A. Baykal, H. Güngünes, S.E. Shirsath, Structural investigation and hyperfine interactions of $BaBi_xLa_xFe_{12-2x}O_{19}$ ($0.0 \le x \le 0.5$) hexaferrites, Cer. Int. 42 (2016) 338–3387.

[12] N. Rezlescu, C. Doroftei, E. Rezlescu, P.D. Popa, The influence of heat-treatment on microstructure and magnetic properties of rare earth substituted $SrFe_{12}O_{19}$, J. Alloy. Compd. 451 (2008) 492–496.

[13] I.A. Auwal, A. Baykal, S. Güner, M. Sertkol, H. Sözeri, Magneto-optical properties $BaBi_xLa_xFe_{12-2x}O_{19}$ ($0.0 \le x \le 0.5$) hexaferrites, J. Magn. Magn. Mater. 409 (2016) 92–98.

[14] I.A. Auwal, S. Güner, H. Güngüneş, A. Baykal, $Sr_{1-x}La_xFe_{12}O_{19}$ ($0.0 \le x \le 0.5$) hexaferrites: synthesis, characterizations, hyperfine interactions and magneto-optical properties, Cer. Int. 42 (2016) 12995–13003.

[15] S. Güner, I.A. Auwal, A. Baykal, H. Sözeri, Synthesis, characterization and magnetooptical properties of $BaBi_xLa_xY_xFe_{12-3x}O_{19}$ ($0.0 \le x \le 0.33$) hexaferrites, J. Magn. Magn. Mater. 416 (2016) 261–268.

[16] M.A. Almessiere, Y. Slimani, A. Baykal, Impact of Nd-Zn co-substitution on microstructure and magnetic properties of $SrFe_{12}O_{19}$ nanohexaferrite, Cer. Int. 45 (2019) 96396–96399.

[17] M. Almessiere, Y. Slimani, A. Korkmaz, S. Guner, M. Sertkol, S.E. Shirsath, et al., Structural, optical and magnetic properties of Tm3+ substituted cobalt spinel ferrites synthesized via sonochemical approach, Ultrason. Sonochem. 54 (2019) 1–10.

[18] Y. Slimania, M.A. Almessierea, A. Demir Korkmaz, S. Guner, H. Güngüneş, M. Sertkol, A. Manikandan, A. Yildiz, S. Akhtar, Sagar E. Shirsath, A. Baykal, $Ni_{0.4}Cu_{0.2}Zn_{0.4}Tb_xFe_{2-x}O_4$ nanospinel ferrites: ultrasonic synthesis and physical properties, Ultrasonics – Sonochem. 59 (2019) 104757.

[19] P. Devendran, T. Alagesan, A. Manikandan, B.S. Asath, K.M. Krishna, S. Rathinavel, K. Pandian, Sonochemical synthesis of $Bi_2S_3$ nanowires using single source precursor and their electrochemical activity, Nanosci. Nanotechnol. Lett. 8 (2016) 478–483.

[20] R.L. Palomino, A.M. Bolarín Miró, F.N. Tenorio, F. Sánchez De Jesús, C.A. Cortés Escobedo, S. Ammar, Sonochemical assisted synthesis of $SrFe_{12}O_{19}$ nanoparticles, Ultrason. Sonochem. 29 (2016) 470–475.

[21] M. Mahdiani, F. Soofivand, M. Salavati-Niasar, Investigation of experimental and instrumental parameters on properties of $PbFe_{12}O_{19}$ nanostructures prepared by sonochemical method, Ultrason. Sonochem. 40 (2018) 271–278.

[22] Y. Slimani, M.A. Almessiere, A. Baykal, AC susceptibility study of Cu substituted $BaFe_{12}O_{19}$ nanohexaferrites, Cer. Int. 44 (2018) 13097–13105.

[23] M.A. Almessiere, Y. Slimani, H. Güngüneş, H.S. El Sayed, A. Baykal, AC susceptibility and hyperfine interactions of vanadium substituted barium nanohexaferrites, Cer Int 44 (2018) 17749–17758.

[24] M.A. Almessiere, Y. Slimani, A. Baykal, Impact of Nd-Zn co-substitution on microstructure and magnetic properties of $SrFe_{12}O_{19}$ nanohexaferrite, Cer. Int. 45 (2019) 963–969.

[25] M. Khandani, M. Yousefi, S.S.S. Afghahi, M.M. Amini, M. Bikhof Torbati, An investigation of structural and magnetic properties of Ce–Nd doped strontium hexaferrite nanoparticles as a microwave absorbent, Mat. Chem. Phys. 235 (2019) 121722.

[26] I.A. Auwal, A. Baykal, H. Güngüneş, Sagar E. Shirsath, Structural investigation and hyperfine interactions of $BaBi_xLa_xFe_{12-2x}O_{19}$ ($0.0 \le x \le 0.5$) hexaferrites, Cer. Int. 42 (2016) 3380–3387.

[27] M.A. Almessiere, Y. Slimani, S. Güner, J. van Leusen, A. Baykal, P. Kögerler, Effect of $Nb^{3+}$ ion substitution on the magnetic properties of $SrFe_{12}O_{19}$ hexaferrites, J. Mater. Sci.: Mater. Electron. 30 (2019) 11181–11192.

[28] M.A. Almessiere, Y. Slimani, H. Gungunes, A. Manikandan, A. Baykal, Investigation of the effects of $Tm^{3+}$ on the structural, microstructural, optical, and magnetic properties of Sr hexaferrites, Results Phys. 13 (2019) 102166.

[29] M.A. Almessiere, Y. Slimani, H.S. El Sayed, A. Baykal, Morphology and magnetic traits of strontium nanohexaferrites: effects of manganese/yttrium co-substitution, J. Rare Earths 37 (2019) 732–740.

[30] M.A. Almessiere, Y. Slimani, N.A. Tashkandi, H. Güngüneş, M. Sertkol, M. Nawaz, S. Ali, A. Baykal, I. Ercan, Tailored microstructures, optical and magnetic qualities of strontium hexaferrites: consequence of $Tm^{3+}$ and $Tb^{3+}$ ions Co-substitution, Ceram. Int. (2019), https://doi.org/10.1016/j.ceramint.2019.07.126.

[31] M.A. Almessiere, Y. Slimani, M. Sertkol, M. Nawaz, A. Baykal, I. Ercan, The impact of Zr substituted Sr hexaferrite: investigation on structure, optic and magnetic properties, Results Phys. 13 (2019) 102244.

[32] M.J. Iqbal, S. Farooq, Impact of Pr–Ni substitution on the electrical and magnetic properties of chemically derived nanosized strontium–barium hexaferrites, J. Alloy. Compd. 505 (2010) 560–567.

[33] Z. Junli, W. Ze, D. Limin, J. Tao, Z. Xianyou, Structural and magnetic behavior of cobalt doped $Ba_{0.5}Sr_{0.5}Fe_{12}O_{19}$ nanoparticles synthesized by chemical co-precipitation technique, App. Mech. Mater. 274 (2013) 406–410.

[34] R. Joshi, C. Singh, D. Kaur, H. Zaki, S.B. Narang, R. Jotania, S.R. Mishra, J. Singh, P. Dhruv, M. Ghimire, Structural and magnetic properties of $Co^{2+}$-$W^{4+}$ ions doped M-type Ba-Sr hexaferrites synthesized by a ceramic method, J. Alloy. Compd. 695 (2017) 909–914.

[35] M.A. Almessiere, Y. Slimani, H.S. El Sayed, A. Baykal, $Ca^{2+}$ and $Mg^{2+}$ incorporated barium hexaferrites: structural and magnetic properties, J. Sol-Gel Sci. Tech. 88 (2019) 628–638.

[36] M.A. Almessiere, Y. Slimani, M. Sertkol, M. Nawaz, A. Sadaqat, A. Baykal, I. Ercan, B. Ozçelik, Effect of $Nb^{3+}$ substitution on the structural, magnetic, and optical properties of $Co_{0.5}Ni_{0.5}Fe_2O_4$ nanoparticles, Nanomaterials 9 (2019) 430.

[37] I. Ali, M.U. Islam, M.S. Awan, M. Ahmad, M.A. Iqbal, Structural and magnetic properties of nano-structured $Eu^{3+}$ substituted M-Type hexaferrites synthesized by sol-gel auto-combustion technique, J. Supercond. Nov. Magn. 26 (2013) 3315–3323.

[38] M.A. Almessiere, Y. Slimani, H. Güngüneş, A. Baykal, N.A. Alhamed, A.V. Trukhanov, S.V. Trukhanov, Structure, Mössbauer and AC susceptibility of strontium nanohexaferrites: effect of vanadium ions doping, Cer. Int. 45 (2019) 11615–11624.

[39] M.A. Almessiere, Y. Slimani, H. Güngüneş, S. Ali, A. Baykal, I. Ercan, AC susceptibility and hyperfine interactions of Mg-Ca ions co-substituted $BaFe_{12}O_{19}$ nanohexaferrites, Cer. Int. 45 (2019) 10048–10055.

[40] M.A. Almessiere, Y. Slimani, S. Güner, A. Baykal, I. Ercan, Effect of dysprosium substitution on magnetic and structural properties of $NiFe_2O_4$nanoparticles, J. Rare Earths 37 (2019) 871–878.

[41] Y. Slimani, M.A. Almessiere, S. Güner, N.A. Tashkandi, A. Baykal, M.F. Sarac, M. Nawaz, I. Ercan, Calcination effect on the magneto-optical properties of Vanadium substituted $NiFe_2O_4$ nanoferrites, J. Mater. Sci.: Mater. Electron. 30 (2019) 9143–9154.

[42] S.J. Gregg, K.S.W. Sing, Adsorption, Surface Area and Porosity, second ed., Academic Press London, UK, 1982.

[43] M. Ramos, G. Berhault, D.A. Ferrer, B. Torres, R.R. Chianelli, HRTEM and molecular modeling of the $MoS_2$-$Co_9S_8$ interface: understanding the promotion effect in bulk HDS catalysts, Catal. Sci. Technol. 2 (2012) 164.

[44] J. Pérez-Ramírez, D. Verboekend, A. Bonilla, S. Abelló, Zeolite catalysts with tunable hierarchy factor by pore-growth moderators, Adv. Funct. Mat. 19 (2009) 3972.